Pure Appl. Geophys. 169 (2012), 1269–1282

DOI 10.1007/s00024-011-0392-1

Pure and Applied Geophysics

Extracting the Virtual Reflected Wavelet from TEM Data Based on Regularizing Method

Guo-qiang Xue,[1] Chao-ying Bai,[2] and Xiu Li[2]

Abstract—A pseudo-seismic interpretation method is an alternative way to process and explain transient electromagnetic (TEM) data, and has become a popular research field in recent years. TEM signals which satisfy the diffusion equation can be converted by means of a mathematical transformation into ones which obey the wave equation. For an ill-posed problem of this kind of transformation, a sub-regularization algorithm is developed in this paper to extract a virtual wavelet of the TEM field. According to the conventional designation of TEM recordings, the entire integration period is divided into seven time intervals. In order to avoid low accuracy in the calculations, high-density wavefield data has been calculated based on the former sub-division. Therefore, the virtual wavelet can be extracted successfully by using an optimized algorithm to obtain high-density integral coefficients for all time windows, and a satisfactory condition number of the coefficient matrix while taking a different channel number in each time period. The Tikhonov regularization inversion scheme is used to determine the optimal parameters based on minimizing a least squares misfit, and the Newton iterative formula is used to obtain optimal regularization parameters. Both synthetic model simulations and a real data interpretation example indicate that the proposed pseudo-seismic wavefield method is a suitable alternative way to interpret TEM data.

Key words: Transient electromagnetic method, wave field transformation, Tikhonov regularization, virtual wavelet.

1. Introduction

The TEM method has been successfully applied to various engineering geological problems (i.e., Buselli *et al.* 1986; Lee and Mcmechan 1987; Chen 1998; Christen and Sorensen 1998; Zhang and Xiao 2000; Xue *et al.* 2004, 2007) and is very suitable for exploring conductive targets buried at depths of up to several hundred meters. With the increased demand for high resolution and accurate subsurface imaging, it is instructive to further investigate TEM processing methodologies to meet the requirements for fine structural interpretation. Since seismic exploration has proved to be the geophysical method offering the highest image resolution and fidelity, it is natural to consider introducing the main ideas of seismic processing into TEM data analysis. This entails converting the TEM field into a pseudo wavefield, and to apply the mature methods of seismic data processing and interpretation to the TEM pseudo wavefield. It is anticipated that the traditional TEM technique will be developed into a multi-channel TEM method (Wright *et al.* 2001; Wright 2003; Ziolkowski 2002, 2005) in the near future, and become a topic of intensive research.

The TEM pseudo-seismic method was first proposed by Weidelt (1972), which at that time was regarded as a new technology to deal with electromagnetic diffusion. Lee and Mcmechan (1987) examined the similarity between electromagnetic waves and seismic waves in term of the governing wave equation. Later they (Lee *et al* 1989) devised a mathematical transformation between the electromagnetic diffusion equation and the pseudo wave equation. Based on the reverse-time migration in seismic exploration, Zhdanov and Booker (1993) and Zhdanov and Portniaguine (1997) developed a reverse-time migration imaging method, which has better performance than traditional TEM methods.

In conventional analysis of electromagnetic data the TEM response is converted into apparent resistivity or apparent vertical conductance, which requires experience on the part of the interpreter. It should be appreciated that there are several forms of apparent resistivity (for example, suitable for early

[1] Key Laboratory of Mineral Resources, Institute of Geology and Geophysics, Chinese Academy of Sciences, Beijing 100029, China.

[2] Department of Geophysics, College of Geology Engineering and Geomatics, Chang'an University, Xi'an 710054, China. E-mail: baicy@chd.edu.cn

time, later time, far field, near field, and so on), which sometimes can result in certain distortions in the above conversion process. However, by transforming the TEM data into a pseudo-wavefield it is possible to offer an alternative way to interpret the TEM data. This uses routine seismic methods, which may increase the reliability of the interpretation, especially when combined with the traditional TEM method.

From the above-mentioned transformation equation one can convert the simulated results obtained from the wave equation related to the conductivity model into the time-domain electromagnetic response signal. But for practical and meaningful interpretation of the TEM data, the necessary process is the reverse one of converting the time-domain electromagnetic response into the simulated pseudo-wavefield related to the wave equation. However, this reverse process is in general ill-conditioned and unstable, so some kind of regularization method should be applied to obtain a better conditioned problem and guarantee a stable transforming process.

The ill-posed problem can be solved by using the Tikhonov regularization procedure constrained by á priori information, or some kind of parameter constraints or weighting factors on the coefficients so that a stable solution can be achieved which is physically meaningful (e.g., Ma and Wang 2005; Wen and Wang 2005; Wang *et al.* 2009). Other popular algorithms for solving the above ill-posed problem are the ridge regression method (Hoerl and Kennard 1970), the linear optimal estimation method based on optimization theory (Hansen and O'Leary 1993), and the optimal parameter estimation scheme based on the minimum RMS (Cai and Grafarend 2000; Cai *et al*. 2001a, b).

In conventional wavefield transformations, the resolution is low due to under sampling in both the time and spatial domains (i.e., Li *et al.* 2005; Xue *et al.* 2007). Therefore, we applied the optimal parameter estimation method, based on the minimum RMS, to convert the electromagnetic wavefield into the pseudo-seismic wavefield. Based on the results of previous studies, we undertook a high-density sampling calculation, in which the high density integral coefficients were calculated through the optimal solution, and the matrix condition numbers for the different samples were obtained. Using Tikhonov regularization based on the minimum RMS, a virtual wavelet can be obtained by using the Newton iterative formula to estimate the optimal regularization parameters. Both synthetic model simulations and a real data interpretation example indicate that this pseudo-seismic wavefield approach is an alternative and practical way to image underground targets.

2. *Wavefield Transform and Integral Coefficients*

The components of the later time TEM field and the pseudo-wavefield can be related in the following way (Lee and McMechan 1987):

$$f(x,y,z,t) = \frac{1}{2\pi t^3}\int_0^\infty \tau e^{\frac{\tau^2}{4t}} u(x,y,z,\tau)d\tau \qquad (1)$$

where, $f(x, y, z, t)$ is a component of the TEM field, and $u(x, y, z, \tau)$ is a corresponding pseudo wavefield, τ is the time of the pseudo-wavefield, which is related to the time t of the TEM field. The discrete form of the above integral is

$$f(x,y,z,t_i) = \sum_{j=1}^{n} u(x,y,z,\tau_j)\cdot a(t_i,\tau_j)\cdot c_j \qquad (2)$$

$$a(t_i,\tau_j) = \frac{1}{2\sqrt{\pi t_i^3}}\tau_j e^{\frac{\tau_j^2}{4t_i}} \qquad (3)$$

where, $a(t_i, \tau_j)$ is the kernel function, which is a rapidly attenuating function with increasing pseudo time τ, and c_j are the integral coefficients. In formula (2) the key issue is to solve for a set of (c_j, τ_j) $(j = 1, 2,\ldots, n)$ that best satisfy this equation.

In order to obtain the solution for the summed version integration of formula (1), we have to find the integral coefficients c_j in formula (2). It is possible to determine the coefficients by using a pair of input–output functions (Anderson 1979). We consider the following expression:

$$\int_0^\infty xe^{-bx^2}d\tau = \frac{1}{2b} \qquad (4)$$

Let $x = \tau$ and $b = \frac{1}{4t}$, and then formula (4) becomes:

$$\frac{1}{2\sqrt{\pi t^3}}\int_0^{\infty}\tau e^{-\frac{\tau^2}{4t}}d\tau=\frac{1}{\sqrt{\pi t}} \tag{5}$$

The discrete form of Eq. (5) is:

$$\sum_{j=1}^{n}\frac{1}{2\sqrt{\pi t_i^3}}\tau_j e^{-\frac{\tau_j^2}{4t_i}}\Delta\tau_j=\frac{1}{\sqrt{\pi t_i}} \tag{6}$$

Comparing with Eq. (3), we can rewrite Eq. (6) as:

$$\sum_{j=1}^{n}a(t_i,\tau_j)c_j=\frac{1}{\sqrt{\pi t_i}} \tag{7}$$

where, $\Delta\tau = c_j$.

By using the optimal method (Li *et al.* 2005; Xue *et al.* 2007), it is possible to select a set of values (c_j, τ_j) ($j = 1, 2,\ldots, n$) from Eq. (7), then substitute them into Eq. (3) for the kernel function $a(t_i, \tau_j)$ and finally obtain the TEM values $f(x, y, z, t_i)$ ($i = 1, 2, \ldots,n$). In order to avoid a large condition number of the coefficient matrix, we divide the total integral time into seven time intervals, which are nearly equal on a logarithmic scale. The time intervals are, in ascending order, 32.5–80.0 μs, 80.0–325.0 μs, 325.0–800.0 μs, 800.0 μs–2.4 ms, 2.4–8.7 ms, 8.7–27.0 ms and from 27.0 to 81.0 ms.

In the computation $\Delta\tau = 1.25$, 6.5, 12.5, 34.0, 165.0, 480.0 and 1420.0 μs for the time intervals 1–7, respectively. Figure 1 depicts the $\tau_j - c_j$ curves in the seven different time intervals. In Fig. 1, the values of the integration coefficients c_j varying with the pseudo time are different among the seven different time intervals, but still exhibit a parabolic form. They range from 0.0067 to 0.0245, 0.0129 to 0.0484, 0.0217 to 0.0741, 0.0344 to 0.1243, 0.0702 to 0.2385, 0.1242 to 0.4314 and 0.2236 to 0.7231 for the seven time intervals, respectively. In practical calculations, some kinds of formulae (such as a parabolic form) are used in sampling according to the above special $\tau_j - c_j$ curve.

3. Regularization Method

Equation (2) can be cast into the form of a matrix equation:

$$F = AU \tag{8}$$

where, $F = (f_i)_n$ and $U = (u_j)_n$ are values of the TEM field and the pseudo wavefield, respectively, and A is the coefficient matrix.

In general, the numerical solution for the above Eq. (8) is unstable and ill-posed, especially when the equation possesses a non-degenerate smooth kernel. To solve such a problem, it is possible to use the Tikhonov regularization method. Based on one of the Tikhonov regularization schemes (Wang *et al.* 2002), the above formula (8) for the ill-posed problem can be rewritten as:

$$\left(A^TA\right)\cdot U = A^TF \tag{9}$$

Its regularized form is given by:

$$\left(A^TA+\alpha(\delta)I\right)\cdot U = A^TF \tag{10}$$

where A^T is the transposed coefficient matrix, $\alpha(\delta)$ is the regularization parameter, which has a trade off effect between the approximation to the wavefield and the stability of the calculation. The quantity I is unit matrix and δ is the error between the computed and the measured data. Hence, there exists an optimal solution for selecting the parameter $\alpha(\delta)$.

Exploiting the regularization theory one can determine the best matching parameter $\alpha(\delta)$, which makes the error between the observed and converted data minimum, according to the error deviation principle (Toint 1981; Gfrerer 1987; Groetsch 1984; Hou and Li 1993) and the residual vector $\eta(\delta, \zeta)$.

The error deviation is:

$$\Delta_\eta(\alpha)=\varphi(\alpha)-\left(\delta+\zeta\left\|U_\alpha^\zeta\right\|_{w^k}\right)^2 \tag{11}$$

where, $\varphi(\alpha)=\left\|A^\zeta U_\alpha^\zeta - F_\delta^\zeta\right\|^2$ is squared error between the magnitudes of the TEM and the converted wavefields. Qunatities δ and ζ are the perturbation errors of Eq. (11) and the coefficient matrix A, respectively. The minimum RMS for the regularization solution can be achieved by directly setting the above error deviation to zero, that is

$$\Delta_\eta(\alpha)=\varphi(\alpha)-\left(\delta+\zeta\left\|U_\alpha^\zeta\right\|_{w^k}\right)^2=0 \tag{12}$$

Equation (12) can be solved by the Newton iterative method. That is, we expand Eq. (12) into a Taylor series at the α_k point,

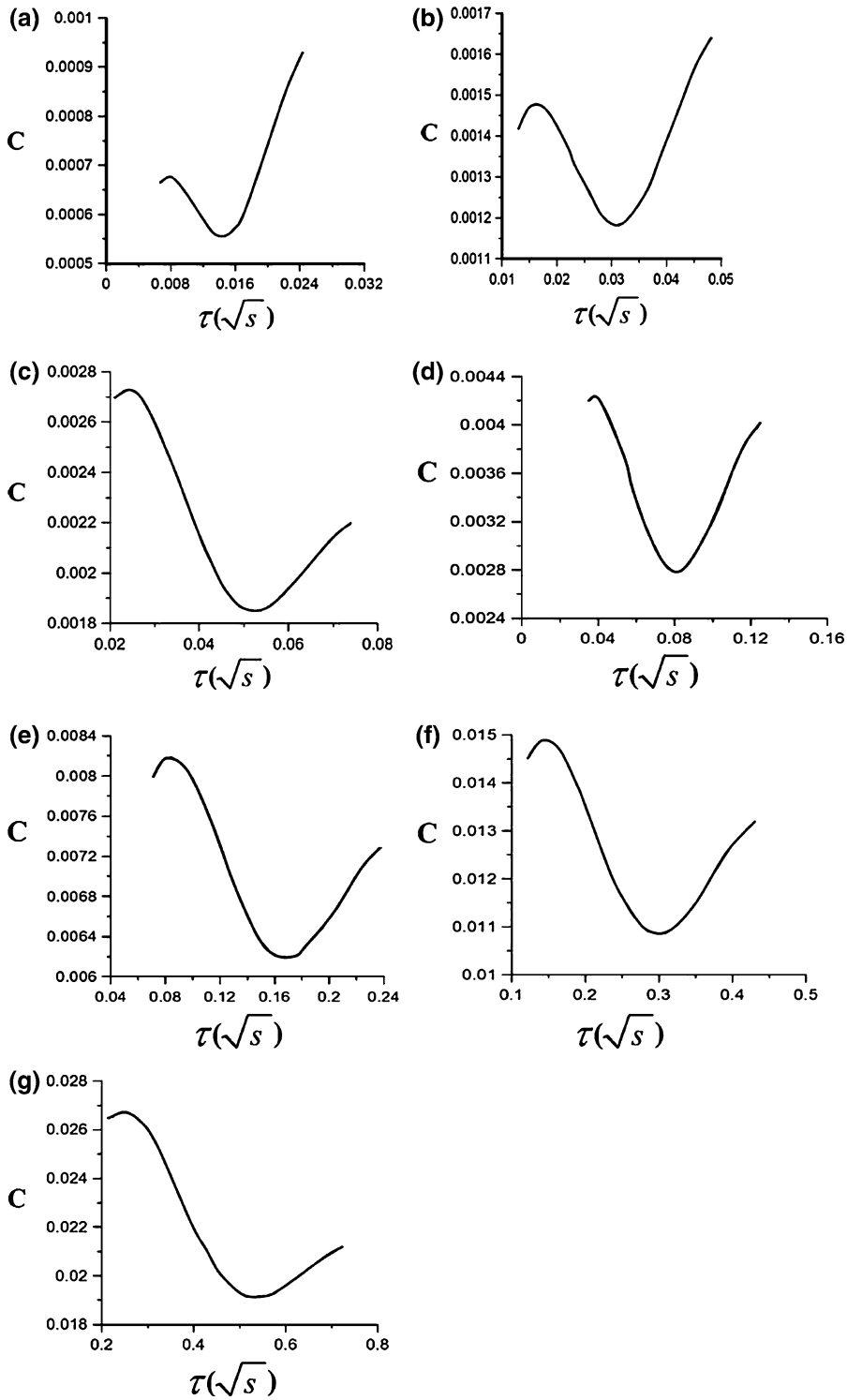

Figure 1
The sampling coordinate–coefficient curve of integration for seven different time intervals (**a**, **b**, **c**, **d**, **e**, **f** and **g** are corresponding results of 1–7 time intervals, respectively)

$$\Delta_\eta(\alpha) = \Delta_\eta(\alpha_k) + \Delta'_\eta(\alpha_k)\Delta\alpha_k = 0 \qquad (13)$$

Furthermore we have,

$$\Delta\alpha_k = -\frac{\Delta_\eta(\alpha_k)}{\Delta'_\eta(\alpha_k)} \quad k = 0,\ 1, \ldots n. \qquad (14)$$

for a given initial value $\alpha_0 > 0$, the $(k+1)$th iterative Newton formula is

$$\alpha_{k+1} = \alpha_k + \Delta\alpha_k = \alpha_k - \frac{\Delta_\eta(\alpha_k)}{\Delta'_\eta(\alpha_k)}, \quad k = 0,\ 1,\ 2, \ldots,\ n \qquad (15)$$

By suitable selection of a regularization parameter α^*, Eq. (12) rapidly converges to zero with a convergence rate of second order.

From Eq. (15) we have:

$$\Delta'_\eta(\alpha) = -\left(\frac{dU_\alpha^\zeta}{d\alpha}\right) U_\alpha^\zeta \left[\alpha + \zeta^2 + \zeta\delta / \left\|U_\alpha^\zeta\right\|_{w^k}\right] \qquad (16)$$

In Eq. (16) the derivative $dU_\alpha^\zeta/d\alpha$ is the solution of the following equation:

$$\left(A_\zeta^T A_\zeta + \alpha \cdot I\right)\xi = -U_\alpha^\zeta \qquad (17)$$

where $\xi = dU_\alpha^\zeta/d\alpha$.

According to the regularization theory, if discrete observed values of the TEM field are given by:

$$F_\delta^\zeta = \left(f_{\delta,0}^\zeta, f_{\delta,1}^\zeta, \ldots, f_{\delta,m}^\zeta\right)^T \text{ and } \left\|F_\delta^\zeta - F^\zeta\right\|_{L^k} \le \delta$$
$$\text{and } \|\bar{A}_\zeta - A_\zeta\| \le \zeta,$$

then the procedure for solving Eq. (1) can be described by the flowchart shown in Fig. 2.

Therefore, one can obtain one regularization parameter for each time interval by using the above error deviation principle and the Newton iterative formula (Li *et al.* 2005; Xue *et al.* 2007). After getting the regularization parameters, it is easy to compute a least-squares solution of the wavefield through Eq. (11).

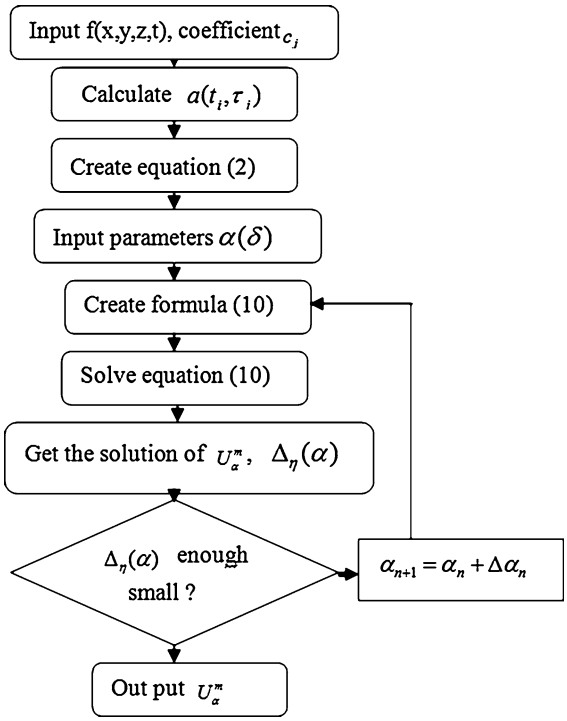

Figure 2
Flowchart for extracting the pseudo-seismic wavelet from TEM data

4. Synthetic Model Simulations

4.1. The Transform from the TEM to the Pseudo-Seismic Wavelet

To validate the above procedure, we first test one synthetic model, which includes three layers having different electrical resistivities and thicknesses, as follows: $\rho_1 = 25\Omega m, H_1 = 60m; \rho_2 = 5\Omega m, H_2 = 60m$ and $\rho_3 = 50\Omega m$. Figure 3a is the decay curve of the secondary TEM induced voltage for the noise-free case, while Fig. 3b is the contaminated decay curve with 10% random noise added. Figure 3c, d are the corresponding converted pseudo wavelets (diagram c: noise-free case and diagram d: contaminated case with 10% random noise added).

From Fig. 3a, b it is clear that the decay curves of the secondary induced voltage are almost the same, regardless of whether noise is added or not. From Fig. 3c, d, the amplitude of the converted pseudo wavelet at early times for the noisy case is the same as for the noise-free case, but small drops in amplitude are noticeable at later times for the noisy case. This is due to the weak amplitudes at later time and the noise being relatively strong. From this test and other tests (not shown here) we have established that the process of waveform transformation is able to preserve the content of the TEM data when the noise level is not very high (say, less than 10%).

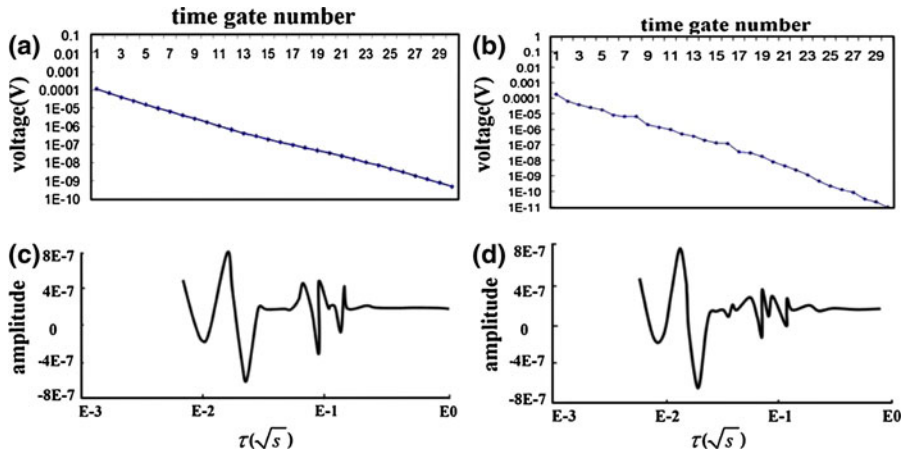

Figure 3
One example of the conversion from traditional TEM to a pseudo-seismic wavelet for a three layered electrical model (**a** decay curve of secondary induction voltage for noise-free case; **b** decay curve of secondary induction voltage for contaminated case with 10% random noise added; **c** converted pseudo-seismic wavelet for noise-free case and **d** converted pseudo-seismic wavelet for contaminated case with 10% random noise added)

4.2. *The Conversion from the TEM to the Pseudo-Seismic Section*

In seismic exploration structure is made visible when the data are arranged into a seismic time section. Here it is possible to convert the TEM data into a pseudo-seismic section. Unlike in seismic exploration, where the velocities are determined by the reflection times from different interfaces, in electromagnetic induction surveys there are no real reflecting interfaces. Therefore, the electromagnetic wave velocity is obtained approximately by the relationship between the propagation time when the electromagnetic disturbance travels through the media, and the electrical parameters of the medium and the frequency of the wave.

The velocity of an electromagnetic wave is given by (KAUFMAN and KELLER 1981):

$$v = \left[\frac{\varepsilon\mu}{2}\left(\sqrt{\left(\frac{\sigma}{\omega\varepsilon}\right)^2+1}+1\right)\right]^{-\frac{1}{2}} \tag{18}$$

where, μ and σ are permittivity, permeability and conductivity of the media, respectively, and ω is angular frequency.

In free space, if we ignore the influence of the conduction current, the velocity of the electromagnetic wave is simple and can be written as:

$$v = {}^{1}/_{\sqrt{\mu\varepsilon}} \tag{19}$$

whereas in conducting media if we omit the influence of the displacement current, then the velocity of the electromagnetic wave reduces to another simple form:

$$v = \sqrt{{}^{2\omega}/_{\mu\sigma}} \tag{20}$$

If we consider a simple case, that is, an averaged velocity $\bar{v}$ could be obtained by taking a reference frequency as $\omega = 1$:

$$\bar{v} = \sqrt{{}^{2}/_{\mu\sigma}} \tag{21}$$

In such situations, the penetration depth is given by :

$$D = \bar{v} \cdot t \tag{22}$$

where t is the delay time (or travel time).

Similarly to seismic exploration, the pseudo layered velocity model can be obtained as $V_i = \sqrt{\frac{2}{\mu_0\sigma_i}}$ The pseudo travel time is calculated from $t_{0i} = \mu_0\sigma_1 d_i^2/N$, where N is the number of layers and d_i is the depth to the bottom of the i-th layer. Furthermore, the converted depth of the i-th layer is determined by $D_i = t_{0i}V_i$, where t_{0i} and V_i are the travel time and velocity of the i-th layer, respectively. After performing a time–depth conversion, the pseudo-seismic wavelets are located at the correct positions of the electrical interfaces. In the data processing the pseudo multiples are muted by an

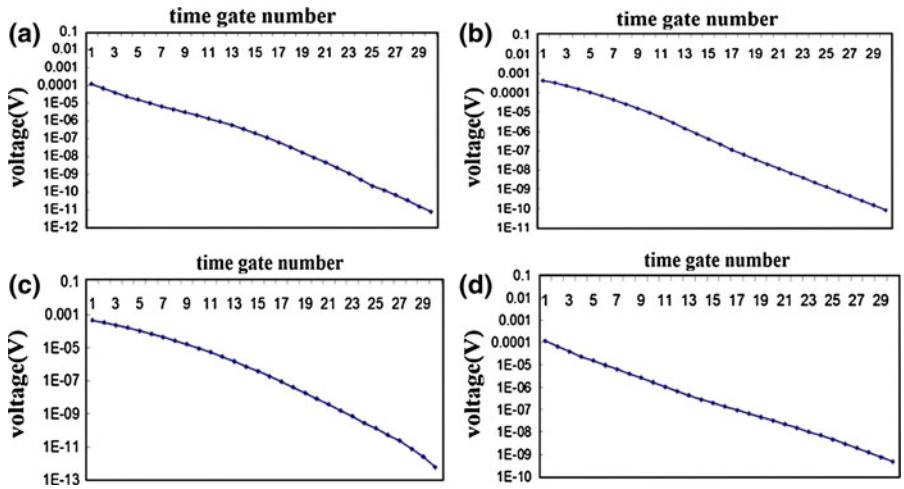

Figure 4
The decay curves of the secondary induction voltage for four different electrical models (**a**, **b**, **c** and **d** for the H, K, A and Q models, respectively)

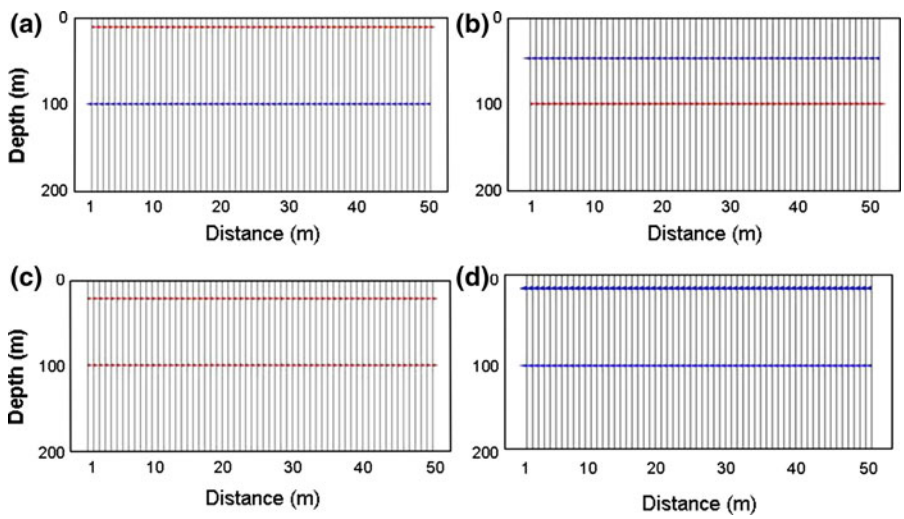

Figure 5
Converted pseudo-seismic sections from four different electrical models (**a**, **b**, **c** and **d** for the H, K, A and Q models, respectively)

algorithm similar to those used in the seismic data processing (WANG *et al*. 1985; LEVY *et al*. 1988).

To validate this conversion, we selected four electrical models (named as H, K, A and Q) having the same total depth, but with the electrical parameters for these models as follows:

$$\textbf{H model}: \quad \rho_1 = 25\Omega \cdot m, \rho_2 = 4\Omega \cdot m, \rho_3 = 36\Omega \cdot m, H_1 = 10m, H_2 = 90m;$$

$$\textbf{K model}: \quad \rho_1 = 25\Omega \cdot m, \rho_2 = 4\Omega \cdot m, \rho_3 = 36\Omega \cdot m; H_1 = 50m, H_2 = 50m;$$

$$\textbf{A model}: \quad \rho_1 = 4\Omega \cdot m, \rho_2 = 16\Omega \cdot m, \rho_3 = 100\Omega \cdot m, H_1 = 25m, H_2 = 75m;$$

$$\textbf{Q model}: \quad \rho_1 = 100\Omega \cdot m, \rho_2 = 36\Omega \cdot m, \rho_3 = 4\Omega \cdot m, H_1 = 20m, H_2 = 100m$$

It is evident that the interpretation to the geoelectrical structure from the decay curves of the secondary induced voltage are not straightforward (see Fig. 4) and it is difficult to distinguish the electrical interfaces. If the electrical decay curves are converted into pseudo-seismic sections (Fig. 5), then

it is clear that all electrical interfaces are distinguished by the pseudo-seismic wavefield, regardless of the electrical models and the layer thicknesses (see the colour wavelet in Fig. 5). From these model simulations and depth conversions, it is reasonable to conclude that the pseudo-seismic wavefield obtained from the TEM wavefield is a practical and an alternative exploration tool for shallow target, in which the electrical properties change.

5. Case Study

There have been many cases of water inrushes, gas explosions and roof collapses associated with the mining process in mainland China. It includes old tunnels, water accumulation, collapsing columns, fire districts, gas accumulations and so on, which have great impacts on the mining industry and local economic development. Over the last two decades the random exploration of small coal mines and the continued excavation of some old mining areas have resulted in many undetermined excavation areas at different levels. Such geological environments pose more potentially dangerous and inconvenient problems for local residents. Hence, it is urgent and also necessary to locate such excavated areas and water inrush regions.

For the above reasons, we selected for our research area the middle part of Shaanxi Province, which is the largest coal mining Province in China (see Fig. 6 for details). The purpose of this study was to apply the above converted pseudo wavefield from the TEM data to detect the characteristics of water inrush areas. The survey region is a low mountainous area with an average elevation of about 1,350 m. The shallow portion of the section to a depth of 20 m is covered by Quaternary loess, and below the rocks are in general Tertiary sandstone, Permian sandstone and mudstone embedded with coal layers and Carboniferous sandstones, mudstones and interbedded coal. The sequence is underlain by Ordovician limestone.

When the coal layers are excavated, there are some hollows at different scales, which results in unstable stress and hence brings stress concentration. Under the action of the overlying rock, deformation, cracking, and dislocation occur, forming a caving zone, fault zone and bent deformation belt. In general, such deformation influences a zone which is significantly larger than the original hollow region. If water causes inrushes, or if surface water leaks through cracks into the excavated areas, then inside

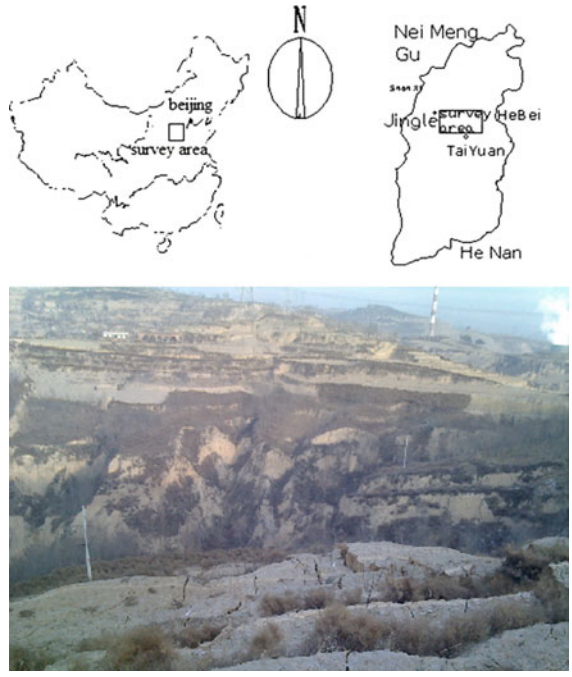

Figure 6
The study region (*Upper left diagram*: Location of Shaanxi Province in mainland China; *Upper right diagram*: Location of the survey region in Shaanxi Province and *Lower diagram*: The topographic review of the survey region)

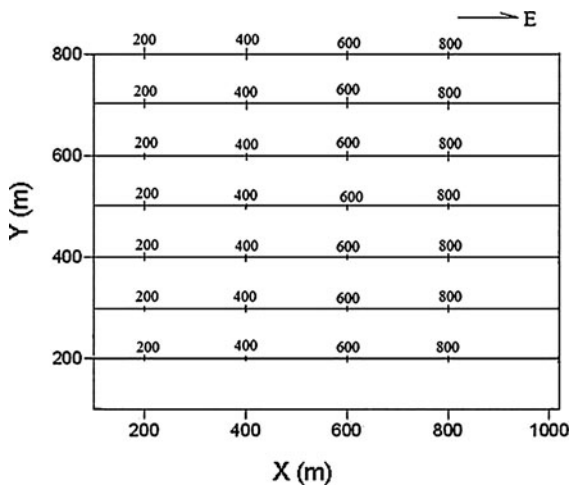

Figure 7
The location of the seven survey lines for the TEM experiment

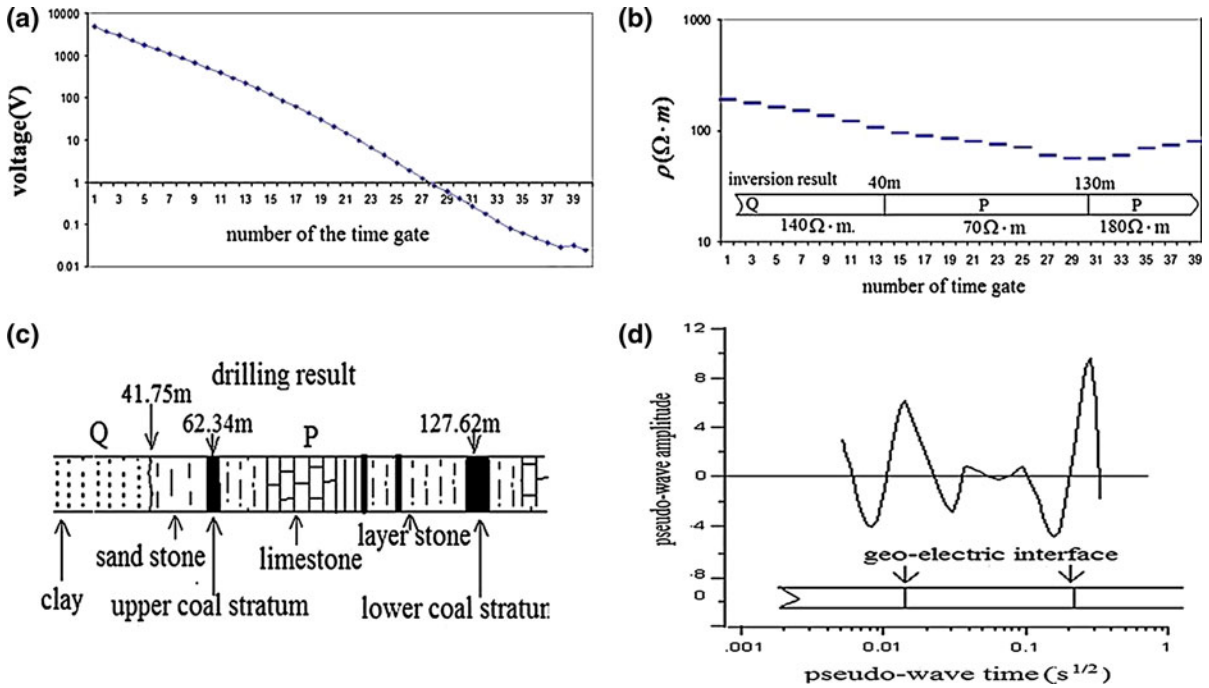

Figure 8
Four different curves for station 400 along line 200 (**a** decay curve of the secondary induction voltage; **b** apparent resistivity curve (*upper panel*) and 1D inversion result (*lower panel*); **c** drilling result and **d** converted TEM pseudo-wavelet)

the hollow the resistivity will change, obviously forming a low resistivity body. This can have a significant resistivity contrast with the surrounding rocks. This is the basic physical foundation for using the TEM method to detect the flooded excavated areas.

In the TEM survey, seven survey lines (at 100 m line interval) and 40 probe points for each line (point interval is 20 m and line length is 1,020 m) were conducted (see Fig. 7 for details).

The instrument used for the data acquisition was an American made GDP-32II electrical workstation. The repetition frequency is 16 Hz, the transmitter loop of size 300 m × 200 m and the current dominant frequency at 70 kHz. In order to validate the pseudo-wavelet interpretation in practical applications and also show an improved imaging resolution, both the traditional (electrical) and the pseudo-seismic section techniques were used in the data process and interpretation.

Figure 8 shows three different curves for station number 400 on line 200 and the drilling information near station 400. Figure 8a is a decay curve of the secondary induced voltage, from which it is difficult to resolve the electrical properties of the ground. Figure 8b shows an apparent resistivity curve (upper panel), from which it may be possible to qualitatively determine the electrical interface. Based on the drilling information near location 400 on line 200 (see Fig. 8c), we performed a 1D inversion of the apparent resistivity curve (upper panel in Fig. 8b) to show the inverted true resistivity section (see lower panel in Fig. 8b). It coincides with the drilling results. Figure 8d is a converted pseudo wavelet, from which it is more visible to determine the electrical interface by inspecting the sudden changes in the wavelet curve. In this case, there are two distinct electrical interfaces, one is around a pseudo time of 0.01 ($s^{1/2}$) and another is near the pseudo time of 0.2 ($s^{1/2}$) (see Fig. 8d).

Figure 9a displays a traditional apparent resistivity contour map in cross section form for line 300. From the figure we see that the apparent resistivity exhibits lateral variations, which indicate that the electrical resistivity is not homogeneous. Between measuring points 420 and 800, there is a low

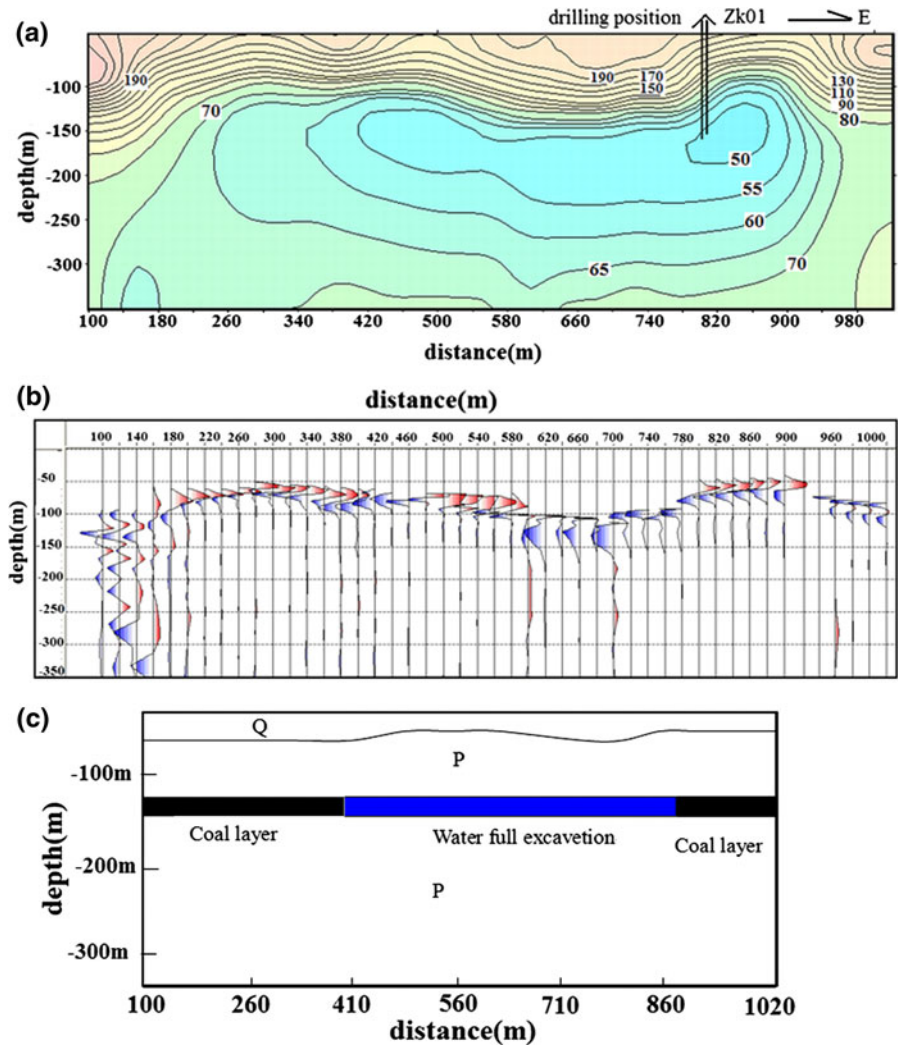

Figure 9
The final results for line 300 (**a** apparent resistivity contour map with an *arrow* indicating later drilling position; **b** the converted pseudo-seismic section and **c** predicted geological section map)

resistivity anomaly below a depth of 120–150 m. Figure 9b is the converted pseudo-seismic section on the same line, in which the coherent events change obviously between the measuring points 420 and 800 at around a depth of 130 m (more precise than those located by the resistivity contour map). Combined with both the apparent resistivity contour map and the pseudo-seismic section, it is reasonable to infer that there may exist a water inrush excavated area between points 420 and 800 below a depth of about 130 m. From the known geological information, the 9th coal layer is located at a depth of 130 m, which coincides with the above location of the anomalous pseudo-seismic section. Therefore, we can infer that the location of the anomalous pseudo-seismic section is a hollow area filled with water (see Fig. 9c). Figure 9c is the interpretation and inversion result based on Fig. 9a, b. Such a conclusion was later verified by the drilling (see Fig. 9a for drilling location). The borehole (named ZK01) was drilled from Feb. 16 to Mar. 13, 2009, to a total depth of 180 m. It was found that between depths of 125.7 and 132.0 m, there exists an excavated area, which closely coincided with the above inference from the TEM survey.

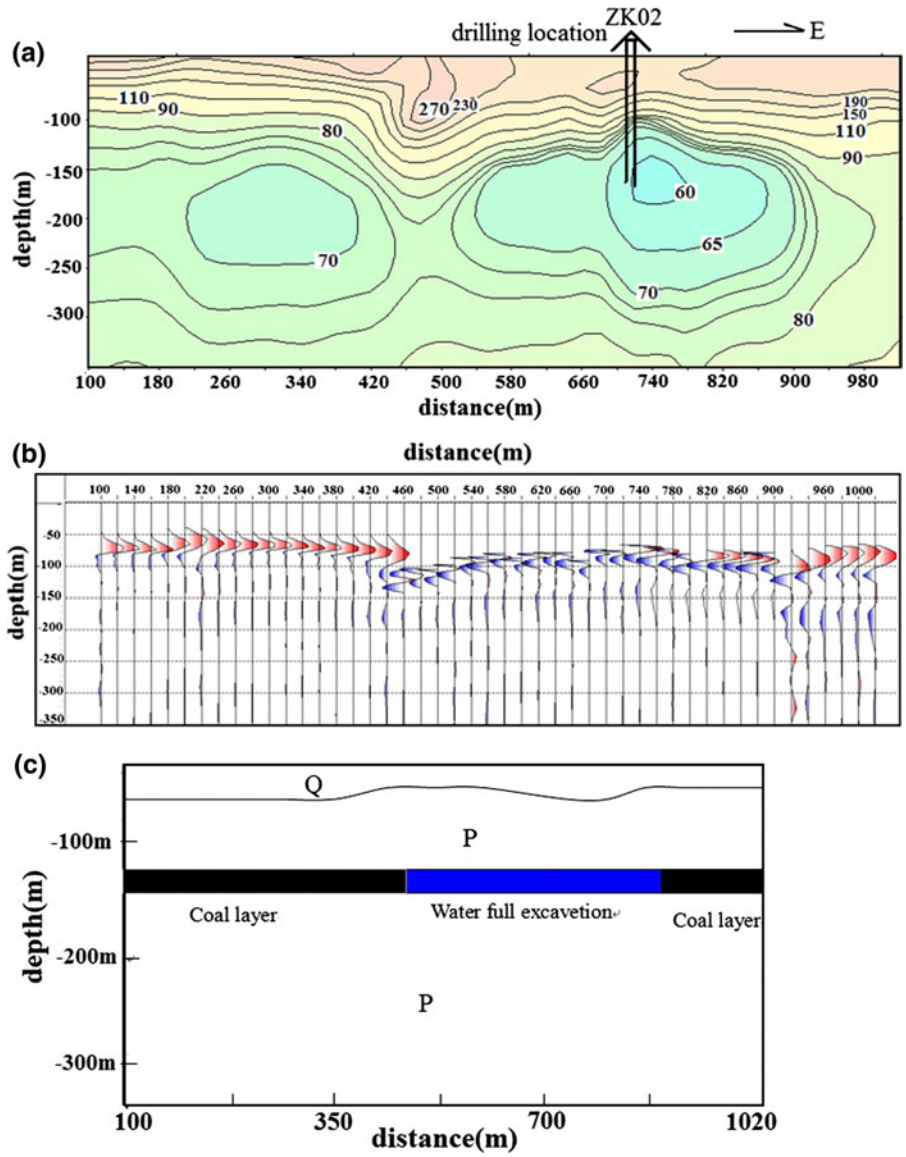

Figure 10
The final results for line 500 line cross section (**a** apparent resistivity contour map with an *arrow* indicating later drilling position; **b** the converted pseudo-seismic section and **c**: predicted geological section map)

Figure 10 shows the results on another survey line (line 500). The apparent resistivity contour map also indicates that the resistivity structure is not uniform but layered (see Fig. 10a). Above a depth of 100 m, the resistivity changes from high to low, while, beneath 100 m depth the resistivity changes from the low to high, indicating the stratification in electrical properties. Between depths of 120 and 150 m, there is a low apparent resistivity anomaly. The pseudo-seismic section on this profile indicates a more accurate location (around 130 m in depth; see Fig. 10b), where the coherent events become discontinuous between stations 440 and 880. Therefore, the same conclusions can also be drawn from the results on line 500 (see Fig. 10c). Figure 10c is the interpretation and inversion result based on Fig. 10a, b. Later drilling tested our inference. The drilling (borehole ZK02, see the location indicated in the

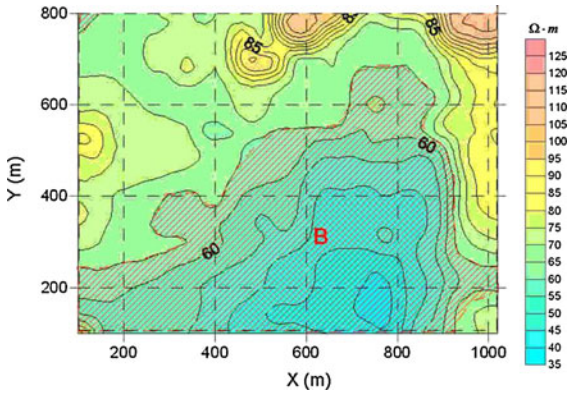

Figure 11
One horizontal apparent resistivity contour map at a depth of 130 m

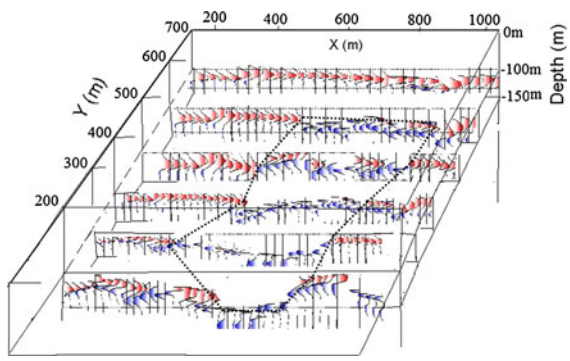

Figure 12
The three-dimensional pseudo-seismic section. In the figure the *blue wavelets* indicate the discontinuous coherent events

Fig. 10a) was conducted from Mar. 13 to Mar. 30, 2009. The total drill depth is 175 m and there exists an excavated area between depths of 116.2 and 125.8 m. This is also closely related to the above inference from the TEM survey.

In order to outline the approximated range of the water inrush excavated area, we show, in Fig. 11, one horizontal apparent resistivity contour map at a depth of 130 m, in which a low resistivity anomalous zone appears in the southeastern part of the survey region. From the resistivity contour map it is difficult to outline the boundary of the water inrush area. Such a problem can be partially resolved by using the pseudo-seismic section (see Fig. 12), in which the boundary of the water inrush excavated area can be determined by the location of the discontinuous coherent events in the pseudo-seismic sections. The

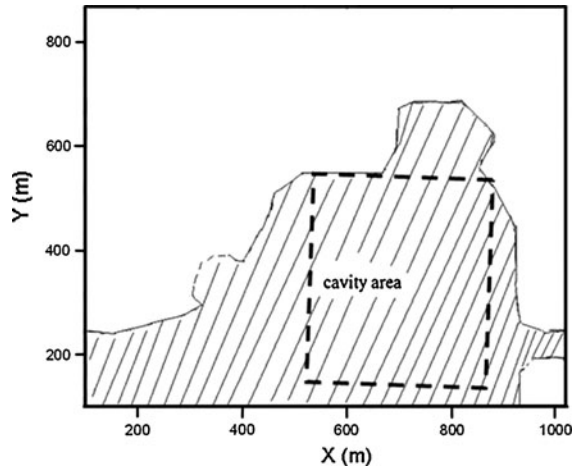

Figure 13
The location of the TEM survey area and the final outline of the water inrush excavated area. In the figure the *upper left panel* is the location of the survey region in mainland China, and the *upper right panel* is the location of the study region in Shaanxi Province. The *lower panel* is the boundary of the water inrush excavated area determined by the apparent resistivity contour (*shadow area*) and by the TEM pseudo-seismic method (*dashed rectangular region*)

locations of the discontinuous events from different survey lines indicate a nearly rectangular region. If we consider that the boundary of the low resistivity anomalous zone is determined, for example, by an apparent resistivity value of 65 $\Omega \cdot m$, then the area of the water inrush excavated area can be outlined, as shown in Fig. 13. Meanwhile, with the pseudo-seismic section the above scale of the water inrush excavated area can be more precisely determined and reduced to a rectangular region. From the above real TEM data interpretation, it is evident that the TEM pseudo-seismic method is advantageous over the traditional TEM method in terms of its location accuracy.

6. Conclusions

With an increased demand for high accuracy interpretation in exploration and improvements in the TEM method itself, it was necessary to devise a new method to accelerate the development so that we have better data interpretation system. The TEM pseudo-seismic data interpretation is currently a hot research topic in the TEM community. In the TEM

pseudo-seismic method, one converts the original signal, which satisfies the diffusion equation of the TEM field, into a virtual wavelet which satisfies the wave equation, through a special mathematical transformation. The inverse process of the above transformation can be classified as a first kind of operator equation, which is an ill-posed and ill-conditioned problem. When discretizing, the formula into linear equation, their orders will increase linearly. For such an ill-posed problem we adopt a subsegment regularization algorithm to extract the TEM pseudo-seismic wavelet. By taking into consideration conventional TEM instrument design, we divided the integral time into seven sub-time intervals, and calculated high dense sampling of the wavefield. Through an optimal solution we obtained the integral coefficients at seven different time intervals, then determined the corresponding regularization parameters using the error deviation principle and the Newton iterative formula, to finally extract the virtual wavelets. Both synthetic model simulations and real data analysis have been used to validate the TEM pseudo-seismic method to be a practical alternative way interpreting TEM data. It should be noted that the transformation from TEM data to a pseudo-seismic wavefield can not increase the information content over the original TEM data. The best thing we can possibly do is to present the pseudo-seismic sections as an alternative (and possibly more visible) interpretation tool to classical inversion of TEM data.

Note that on the scientific side, no mathematical transformation can overcome the fundamental limitations of diffusion physics and improve resolution. This was not a revolutionary new approach to TEM interpretation via TEM pseudo-seismic method, but provided an equivalent of seismic-like imaging method. Nowadays, 2D/3D TEM surveying has become more and more fashionable, while in some cases one dimensional accurate interpretation is still necessary. For example, in mining and oil exploration, the target can be regarded as a 1D electrical model. In such cases, it is worthwhile to further develop the TEM method and improve the methodology itself. Based on the 1D TEM exploration, it is more reliable to conduct the 2D/3D TEM exploration for the future.

Acknowledgments

This research works were jointly supported by the National Natural Science Foundation (project no: 40774020, 40774066 and 41030750) and Chinese Academy of Sciences Innovation Fund (KZCX2-YW-Q04-07).

References

Anderson,W. L., 1979. *Computer Program: Numerical integration of related Hankel transforms of orders 0 and 1 by adaptive digital filtering*. Geophysics, *44*(7), 910–918.

Buselli, G., McCracken, K. G. and Thorburn, M., 1986. *Transient electromagnetic response of the teutonic bore ore body*. Geophysics, *51*(4), 957–963.

Cai, J. and Grafarend, E., 2000. The sample distribution of the sample means and sample variance-covariance of a three dimensional, symmetric rank two random tensor (strain, stress), Geodetic Week, Potsdam, 10–12. October.

Cai, J., Grafarend, E. and Schaffrin, B., 2001a. The a-weighted BLE of the direct observations of a symmetric random tensor, Simulated case study: 2-dimensional strain, Geodetic Week, Köln, 18–21. September.

Cai, J., Grafarend, E. and Schaffrin, B., 2001b. The $\sum$ −BLUUEof eigenspace components of a symmetric random tensor of second order, Simulated case study: 2-dimensional strain, Geodetic Week, Köln, 18–21. September.

Chen, C. S., 1998. *Mapping plate boundaries using TEM method along the longitudinal, Taiwan*. Geophysics, *63*(3), 868–879.

Christen, N. B. and Sorensen, N. K. I., 1998. *Surface and borehole electric and electromagnetic method for hydrogeological investigation*. Eur. J. Environ. Eng. Geophys., *3*, 75–90.

Gfrerer, H., 1987. *An aposteriori parameter choice for ordinary and iterated Tikhonov regularization leading to optimal convergence rates*. Math. Comp., *49*(180), 507–522.

Grafarend, E W., 1993. Ausgleichungrechnung inlinearen Modellen. Bibliographisches Institut Wissen-schaftsverlag, Mannheim.

Groetsch, C. W., 1984. The Theory of Tikhonov Regularization for Fredholm Equation of the First Kind, Pitman Advanced Publishing Program, Boston.

Hansen, P. C. and O'Leary, D. P., 1993. *The use of the L-curve in the regularization of discrete ill posed problems*. SIAM Journal on Scientific Computing, *14*(6), 1487–1503.

Hoerl, A. E. and Kennard, R. W., 1970. *Ridge egression: biased estimation for non-orthogonal problems*. Technometrics, *12*(1), 55–67.

Hou, Z. Y., Li, H. N., 1993. *The general arcangeli's method for solving ill-posed Problems*. Non linear Analysis, *21*(3), 197–206.

Kaufman A. A. and Keller G.V., 1981. The magnetotelluric sounding method. Elsevier Science Publishing Co.

Lee, S. and Mcmechan, G A., 1987. *Phase-field imaging: The electromagnetic equivalent of seismic migration*. Geophysics, *52*(5), 678–693.

Lee K H. Liu G, Morrison H F. *A new approach to modeling the electromagnetic response of conductive media*. Geophysics, 1989, *54*(6): 1180–1192.

Levy, S., Oldenburg, D., Wang, J., 1988. *Subsurface imaging using magnetotelluric data*. Geophysics, *53*(1), 104–117.

Li, X., Xue, G. Q., Song, J. P., Guo, W. B. and Wu, J.J., 2005. *The Optimization of Transient Electromagnetic Field–Wave Field Conversion*. Chinese J. Geophysics (in Chinese), *48*(5), 1185–1190.

Ma, Q. H. and Wang, Y. F., 2005. *Iterative implementation of the adaptive regularization yields optimality*. Science in China Ser. A, *48*(4), 485–492.

Tikhonov, A, N., Arsenin, V. Y., Tikhonov, A. N., et al., 1977. Solutions of ill-posed problems. New York: Wiley.

Toint, Ph. L., 1981. Towards an efficient sparsity exploiting Newton method for minimization, in sparse matrices and their uses (ed, Duff, I.), Berlin: Academic Press.

Xue, G. Q., Song, J. P. and Yan, S., 2004. *Detecting shallow caverns in China using TEM*. The Leading Edge, *23*(7), 694–695.

Xue, G. Q., Yan, Y. J., Li, X. and. Di, Q. Y., 2007. *Transient electromagnetic S-inversion in tunnel prediction*. Geophys. Res. Lett., *34*, L18403.

Xue G. Q., Yan,Y. J. and Li, X., 2007. *Pseudo-seismic wavelet transformation of transient electromagnetic response in geophysical exploration.* Geophys. Res. Lett., *34*, L16405, doi: 10.1029/2007GL031116.

Weidelt, P., 1972. *The inverse problem of geomagnetic induction: Zeit. für* Geophys., *38*, 257–298.

Wang, J. Y., Oldenburg, D., Levy, S., 1985. *Pseduo-sesmic interpretation method of MT*. Oil Geophysical Exploration (in Chinese), *20*(1), 66–79.

Wang, Y. F., Yuan, Y. X., Zhang, H. C., et al., 2002. *A trust region-CG algorithm for delurring problem in atmospheric image reconstruction.* Science in China, Ser. A, *45*:731–740.

Wang, Y. F., Cao, J. J., Yuan, Y. X., Yang, C. C. and Xiu, N. H., 2009. *A regularizing active set method for ill-posed multichannel image restoration problem*. Applied Optics, *48*, 1389–1401.

Wen, Z. W. and Wang, Y. F., 2005. *A new trust region method for image restoration*. Science in China Ser. A, *48*(2), 169–184.

Wright, D. A., 2003. Detection of hydrocarbons and their movement in a reservoir using time-lapse multi-transient electromagnetic _MTEM_ data. PhD thesis, University of Edinburgh.

Wright, D. A., Ziolkowski, A. and Hobbs, B. A., 2001. Hydrocarbon detection with a multichannel transient electromagnetic survey. 71st Annual International Meeting, SEG, Expanded Abstracts, 1435–1438.

Zhang, Z. and Xiao, J., 2000. *Inversion of surface and borehole data from large loop transient electromagnetic system over a 1-D Earth*. Geophysics, *66*(4), 1090–1096.

Zhdanov, M. S. and Booker, J. R., 1993. Underground imaging by electromagnetic migration. In 63rd Ann. Internat. Mtg. Expl. Geophys., Expanded Abstracts, 355–357.

Zhdanov, M. S. and Portniaguine, O., 1997. *Time-domain electromagnetic migration in the solution of inverse problems*. Geophys. J. Int., *131*, 293–309.

Ziolkowski, 2002. *Hydrocarbon detection and monitoring with a multichannel transient electromagnetic MTEM survey*. The Leading Edge, *21*, 852–864.

Ziolkowski, 2005. Detection of subsurface resistivity contrasts with application to location of fluids. US Patent 6 914 433.

(Received November 10, 2010, revised June 17, 2011, accepted July 4, 2011, Published online August 9, 2011)